Full Length Article

Strength and failure characteristics of marble spheres subjected to paired point loads

Rui Zhao [a], Ming Tao [a,*], Wenzhuo Cao [b], Kun Du [a], Jianbo Zhu [c]

[a] School of Resources and Safety Engineering, Central South University, Changsha, China
[b] Department of Earth Science and Engineering, Imperial College London, London, UK
[c] Guangdong Provincial Key Laboratory of Deep Earth Sciences and Geothermal Energy Exploitation and Utilization, College of Civil and Transportation Engineering, Shenzhen University, Shenzhen, China

ARTICLE INFO

ABSTRACT

Failure of irregular rock samples may provide implications in the rapid estimation of rock strength, which is imperative in rock engineering practice. In this work, analytical, experimental and numerical investigations were carried out to study the mechanical properties and failure characteristics of rock spheres under paired point loads. Analytical solutions indicted that with the increase in sample size (contact angle) and decrease in Poisson's ratio, the uneven tensile stress in theta direction decreased. Then laboratory experiments were carried out to investigate the load characteristics and failure mode of spherical marble samples with different sizes subjected to a pair of diametral point loads. The discrete element method (DEM) was adopted to study the failure process of rock spheres. The effect of the sphere diameter on the point load contact angle was examined in terms of peak load, crushed zone distribution and energy dissipation. Experimental and numerical results showed that the samples primarily fail in tension, with crushed zones formed at both loading points. With increase in the sample size, the contact angle, crushed area and total work increase. As the specimen diameter increases from 30 mm to 50 mm, the peak load on the specimen increases from 3.6 kN to 8.8 kN, and the percentage of crushed zone (ratio of crushing zone to sample radius, d/r) increased from 0.191 to 0.262. The results of the study have implications for understanding the failure of irregular rock specimens under point loading conditions and their size effects.

© 2023 Institute of Rock and Soil Mechanics, Chinese Academy of Sciences. Production and hosting by Elsevier B.V. This is an open access article under the CC BY-NC-ND license (http://creativecommons.org/licenses/by-nc-nd/4.0/).

1. Introduction

Rocks, as a complex and widespread natural material, are diverse in their mechanical behavior (Azarafza et al., 2019). The acquisition and determination of physico-mechanical parameters, such as compressive strength and tensile strength for rock mass, are of great importance to geotechnical engineering design. Many methods have been proposed to obtain the mechanical parameters of rocks. Du et al. (2020) systematically summarized the methods for obtaining static mechanical parameters of rocks in laboratory.

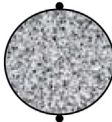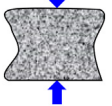The rapid and accurate acquisition of mechanical parameters of rocks is essential for the construction and classification of rock quality. The tensile strength of rock is of paramount importance in the tensile failure associated with a wide range of underground hazards. Thus, the tensile strength is a fundamental indicator. Scholars have developed numerous methods to obtain the tensile strength of rocks, including direct and indirect tensile tests (Brown, 1981; Du et al., 2020). The indirect tensile tests are easier to implement and are thus widely used to obtain rock tensile strength and uniaxial compressive strength (UCS) in field and laboratory (Şahin et al., 2020; Garrido et al., 2021). Examples of indirect tensile tests include irregular point load strength tests (Franklin, 1985; Akbay and Altindag, 2020; Fan et al., 2021) and Brazilian tests. These typical methods for obtaining the tensile strength of rock and their advantage and disadvantage were listed in Table 1. Among them, the point load test is the fastest and does not require specimen processing. It has been found that the UCS of rock is related to the point-load strength (Garcia-Fernandez et al., 2018). According to this, AlAwad (2020) improved the relationship between the two mechanical parameters by introducing Poisson's

Table 1
Typical methods for obtaining the tensile strength of rock.

Method	Equipment	Schematic diagram	σ_t	Advantage	Disadvantage
Direct tensile test	Mechanical test system		F/A	High accuracy Suitable for almost all rock types	Complex sample processing Time-consuming experimental process
Brazilian indirect tension test	Mechanical test system		$2F/(\pi Dt)$	High accuracy Suitable for homogeneous rock masses	Complex specimen processing
Point load test	Hydraulic point load tester		Empirical fitting or $1.4F/a^2$	Fast Wide range of applicability No specimen processing	Low accuracy

Note: F is the peak load, D is the diameter of the disc, t is the thickness, σ_t is the tensile strength, and a is the half of the distance between the load points.

ratio as a correction factor. It is generally believed that the UCS of rock is proportional to the point load index (Franklin, 1985) and the size of sample also has a great influence on point load index (Russell and Muir Wood, 2009). The Brazilian disc tests have been widely used in testing for both brittle rock (Garcia-Fernandez et al., 2018) and weak rock (Rabat et al., 2020). Extensive efforts have been made on experimental and analytical investigations on the Brazilian disc tests. Li and Wong, 2012 simulated the stress and strain distribution in Brazilian disc tests using FLAC3D, and the numerical results were consistent with theoretical and experimental results (Markides and Kourkoulis, 2012). However, few point load strength tests have been conducted on samples in other shapes, such as sphere. Hiramatsu and Oka (1966) gained the stress distribution of the spherical and disc-shaped samples under point loads through three-dimensional (3D) photoelastic tests, and the close form solution of the stress distribution in a sphere under point loads was given. Moreover, a formula for calculating the tensile strength of spherical rock based on point loads was proposed. In the next few decades, many scholars have studied point loads on rocks, mainly focusing on determining the relationship between point load indicators and strength parameters of rocks. Wijk (1980) developed an eight-point circumferential point load equipment, and carry out experiments on spherical and cylindrical samples. The experimental results showed that the multi-point load index was greater than the single-point load index. Russell and Muir Wood (2009) theoretically established the relationship between point load index, UCS and tensile strength of rock. They presented a theoretical expression of the correlation coefficient C as a function of contact angle, loading device, and rock material properties. The results were in good agreement with the actual UCS and tensile strength obtained from experiments. Chau (1998), Chau and Wei (1999), and Wei and Chau (2013) have further derived the analytical solutions of stress distribution for different shaped samples (i.e. isotropic sphere and cylinder) under point loads. The results pointed out that the stress inhomogeneity induced by anisotropy occurs at the center of the specimen. As a way of quickly obtaining mechanical parameters of rocks, Brazilian disc test has been extensively studied in terms of damage pattern of Brazilian discs.

Since the 2010s, novel techniques (i.e. digital image correlation technology) have provided new insights on the investigation on rock failure process (Sgambitterra et al., 2018). For instance, Li et al. (2020) obtained the failure modes of five different rock samples in Brazilian disc tests by the digital image correlation technique with flat loading platens; flat loading platens with two small-diameter steel rods and curved loading jaws, experimentally assessed the damage patterns and crack initiation in Brazilian discs under different loading conditions. The damage pattern of specimen was determined by the stress distribution. Therefore, in the Brazilian disc test, crack initiation and damage patterns are used to determine whether an experiment is suitable for assessing the mechanical properties of a material. For example, central cracking is thought to be caused by tensile stresses and the experiment is successful. Compared with experimental studies on Brazilian disc tests, point load tests on rock spheres are fewer because of the difficulty in fabricating spherical-shaped samples.

Paired point load experiments on spheres can be equated to point loading experiments on irregular rock masses. Thus, this study provides a reference for failure mode under point loads of irregular rock masses to determine mechanical parameters. In this study, the point load experiments on different sizes of marble spheres were carried out, and the impact of sample size on failure mode was evaluated. Based on the experimental results, the influence of size on contact angle and failure mode is obtained. Meanwhile, the discrete element method-based (DEM-based) software PFC^{3D} was used to simulate the failure process of rock spheres under point loads and the failure mode were analyzed.

2. Analytical solution of stress distribution within an elastic sphere under point loads

Assuming that an isotropic elastic sphere is subjected to a pair of diametral point loads (Fig. 1), it is convenient to analyze the stress distribution of any individual point represented in terms of (r, θ, φ) in a polar spherical coordinate system, as shown in Fig. 2.

By omitting the body force of the solid sphere, the three stress components satisfy the following equations (Chau and Wei, 1999):
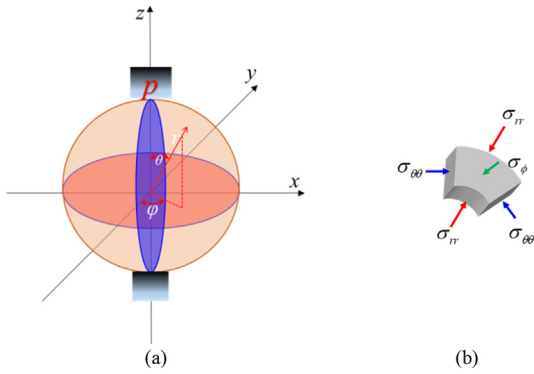
Fig. 1. (a) Polar spherical coordinate system used for stress analysis of a sphere under (b) a pair of diametral point loads and stress components. r is the radial coordinate; and θ and φ are the polar and azimuthal angles, respectively.

$$\left.\begin{array}{l} \dfrac{\partial \sigma_{rr}}{\partial r}+\dfrac{1}{r}\dfrac{\partial \tau_{r\theta}}{\partial \theta}+\dfrac{1}{r}(2\sigma_{rr}-\sigma_{\theta\theta}-\sigma_{\varphi}+\tau_{r\theta}\cot\theta)=0 \\[2mm] \dfrac{\partial \tau_{r\theta}}{\partial r}+\dfrac{1}{r}\dfrac{\partial \sigma_{\theta\theta}}{\partial \theta}+\dfrac{1}{r}[(\sigma_{\theta\theta}-\sigma_{\varphi})\cot\theta+3\tau_{r\theta}]=0 \\[2mm] \dfrac{\partial \tau_{\varphi r}}{\partial r}+\dfrac{1}{r}\dfrac{\partial \tau_{\theta\varphi}}{\partial \theta}+\dfrac{1}{r}(3\tau_{r\varphi}+2\tau_{\theta\varphi}\cot\theta)=0 \end{array}\right\} \tag{1}$$

where σ_{rr} is the stress in r-direction; $\sigma_{\theta\theta}$ is the stress in θ-direction; and $\tau_{r\theta}$, $\tau_{\varphi r}$, $\tau_{r\varphi}$ and $\tau_{\theta\varphi}$ are the shear stress at each direction.

The stress boundary conditions of the sphere can be expressed by (Wei and Chau, 2013):

$$\left.\begin{array}{l} (\sigma_{rr})_{r=a}=p \quad (0\leq\theta\leq\theta_0,\pi-\theta_0\leq\theta\leq\pi) \\ (\sigma_{rr})_{r=a}=0 \quad (\theta_0<\theta<\pi-\theta_0) \end{array}\right\} \tag{2}$$

$$\sigma_{r\varphi}=\sigma_{r\theta}=0 \quad (r=a) \tag{3}$$

where a is the radius of sphere, F is the peak load at the ends of the sphere, and p is the stress given by the following function of the peak load F and the contact angle θ_0 subtended at the center of the sphere by the loaded area:

$$p=F\Big/\left[2\pi a^2(1-\cos\theta_0)\right] \tag{4}$$

As illustrated in Fig. 2, θ_0 is the contact angle which can be expressed as
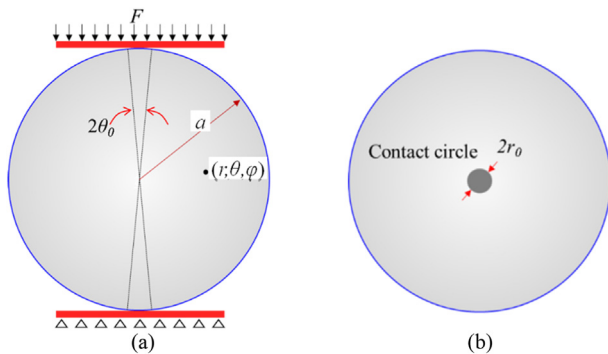

Fig. 2. Schematic diagrams of a rock sphere under a pair of diametral point loads: (a) Front and (b) top views. r_0 is the radius of the contact circle.

$$\theta_0=\arcsin(r_0/a) \tag{5}$$

Then the stress p can be expressed as (Russell and Muir Wood, 2009):

$$p=F\Big/\left(2\pi r_0{}^2\right)=\frac{F}{2\pi\sin^2(\theta_0)a^2} \tag{6}$$

The stress distribution inside the sphere subjected to a pair of diametral point loads was given by Hiramatsu and Oka (1966) as follows:

$$\sigma_{rr}=p(1-\cos\theta_0)+p\sum_{n=1}^{+\infty}\frac{(4n+1)[\cos\theta_0 P_{2n}(\cos\theta_0)-P_{2n-1}(\cos\theta_0)]}{(8n^2-8n+3)\lambda+(8n^2+4n+2)\mu}$$
$$\cdot\left\{\left[\left(4n^2-2n-3\right)\lambda+(2n+1)(2n-2)\mu\right]\left(\frac{r}{a}\right)^{2n}\right.$$
$$\left.-\frac{2n}{2n+1}\left[2n(2n+2)\lambda+\left(4n^2+4n-1\right)\mu\right]\left(\frac{r}{a}\right)^{2n-2}\right\}P_{2n}(\cos\theta) \tag{7}$$

$$\sigma_{\theta\theta}=p(1-\cos\theta_0)+p\sum_{n=1}^{+\infty}\frac{(4n+1)[\cos\theta_0 P_{2n}(\cos\theta_0)-P_{2n-1}(\cos\theta_0)]}{(8n^2-8n-3)\lambda+(8n^2+4n+2)\mu}$$
$$\cdot\left\{-[(2n+3)\lambda-(2n-2)\mu]\left(\frac{r}{a}\right)^{2n}-\frac{(8n^3-8n^2)\lambda+\left(8n^3+8n^2-2n\right)\mu}{(2n-1)(2n-1)}\right.$$
$$\left.\cdot\left(\frac{r}{a}\right)^{2n-2}\right\}P_{2n}(\cos\theta)+p\sum_{n=1}^{+\infty}\frac{(4n-1)[\cos\theta_0 P_{2n}(\cos\theta_0)-P_{2n-1}(\cos\theta_0)]}{(8n^2+8n+3)\lambda+(8n^2+4n+2)\mu}$$
$$\cdot\left[\frac{(2n+3)\lambda+(2n+5)\mu}{(2n+1)}\left(\frac{r}{a}\right)^{2n}-\frac{8n^2\lambda-\left(4n^2-4n-1\right)\mu}{4n^2-1}\left(\frac{r}{a}\right)^{2n-2}\right]$$
$$\cdot\frac{n^2}{(4n+1)\sin\theta}\left[n^2 P^1_{2n+1}(\cos\theta)-(n+1)^2 P^1_{2n-1}(\cos\theta)\right] \tag{8}$$

$$\sigma_{\varphi}=p(1-\cos\theta_0)+p\sum_{n=1}^{+\infty}\frac{(4n+1)[\cos\theta_0 P_{2n}(\cos\theta_0)-P_{2n-1}(\cos\theta_0)]}{(8n^2+8n+3)\lambda+(8n^2+4n+2)\mu}$$
$$\cdot\left\{-[(2n+3)\lambda-(2n-2)\mu]\left(\frac{r}{a}\right)^{2n}-\frac{4n^2(2n+2)\lambda-2n\left(4n^2-4n-1\right)\mu}{(2n-1)(2n+1)}\right.$$
$$\left.\cdot\left(\frac{r}{a}\right)^{2n-2}\right\}P_{2n}(\cos\theta)-p\sum_{n=1}^{+\infty}\frac{(4n+1)[\cos\theta_0 P_{2n}(\cos\theta_0)-P_{2n-1}(\cos\theta_0)]}{(8n^2+8n+3)\lambda+(8n^2+4n+2)\mu}$$
$$\cdot\left[\frac{(2n+3)\lambda+(2n+5)\mu}{2n+1}\left(\frac{r}{a}\right)^{2n}-\frac{(4n^2+2n)\lambda+(2n-1)^2\mu}{4n^2-1}\left(\frac{r}{a}\right)^{2n-2}\right]$$
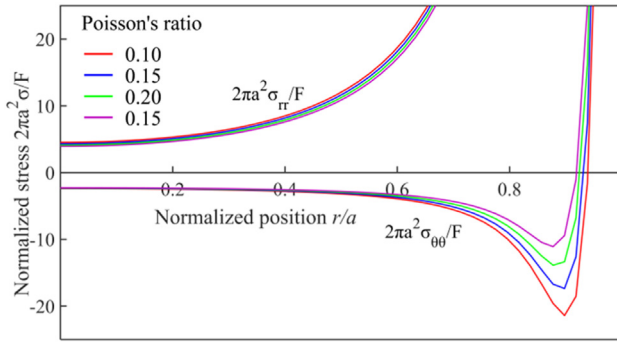$$\cdot\cos\theta P^1_{2n}(\cos\theta) \tag{9}$$

Fig. 3. Influence of Poisson's ratio on the normalized stress $2\pi\sigma a^2/F$ distribution inside the sphere ($\theta_0 = 1°$, all stresses are normalized with $F/(2\pi a^2)$).

$$\tau_{r\theta} = p \sum_{n=1}^{+\infty} \frac{(4n+1)[\cos\theta_0 P_{2n}(\cos\theta_0) - P_{2n-1}(\cos\theta_0)]}{(8n^2+8n+3)\lambda + (8n^2+4n+2)\mu} +$$
$$\frac{(4n^2+2n)\lambda - 2n(4n^2-4n-1)\mu}{(2n+1)} \left[\left(\frac{r}{a}\right)^{2n} - \left(\frac{r}{a}\right)^{2n-2}\right] P_{2n}^1(\cos\theta) \tag{10}$$

$$\sigma_{\theta\varphi} = \sigma_{\varphi r} = 0 \tag{11}$$

where n is a positive integer, λ and μ are the Lame's constants of rocks, and $P_n(\cdot)$ is the Legendre's polynomial of the first kind. In order to standardize the stress components, the dimensionless normalized stress is introduced, which is defined as σ/p and can also be written as $2\pi\sigma a^2/F$. According to Eqs. 7–11, the distributions of normalized maximum and minimum principal stresses in the central vertical cross-section along the loading direction are shown for various contact angles and Poisson's ratios in Figs. 3 and 4, respectively.

The contact angle and Poisson's ratio affect the stress distribution, in particular tensile stress distribution, near the loading points. With the increases in Poisson's ratio and contact angle, the maximum tensile stress reduces near the loading point at both sides.

3. Diametral point loading experiment and analysis

In Section 2, the stress distribution obtained from analytical solutions was presented. Based on the analytical results, Hiramatsu and Oka (1966) proposed that one or two of the following failure mo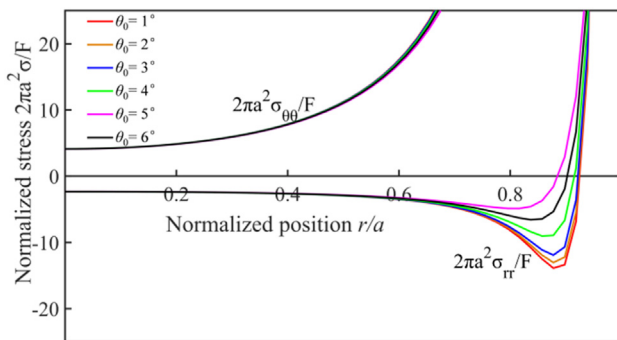des occur: (i) tension failure in the middle part due to the angular stress at $\theta = 0$, $(\sigma_{\theta\theta})_{\theta=0}$; (ii) crushing failure due to compression radial and angular stress at $\theta = 0$, $(\sigma_{rr})_{\theta=0}$ and $(\sigma_{\theta\theta})_{\theta=0}$ near the loading points; and (iii) macroscopic shear failure over the whole sample due to radial stress at $\theta = 0$, $(\sigma_{rr})_{\theta=0}$. Herein, to evaluate the failure characteristics of rock spheres under paired point loads, experiments on marble spheres in different diameters will be presented in this section.

3.1. Sample preparation and experimental procedure

All the samples used in the experiment were taken from the same block of marble with uniform texture and no obvious primary defects. Before sample preparation, the basic mechanical parameters of the rock were measured. The UCS value is around 110 MPa, and the tensile strength obtained from Brazilian tests is 3.7 MPa. The density, Poisson's ratio and elastic modulus are 2635 kg/m^3, 0.2 and 9.5 GPa, respectively. Several cylindrical samples were first drilled from the same marble block along the same sampling direction, and then fabricated to the spherical shape by specified carving equipment. The fabrication was controlled in a manner that the blade moved around the samples to cut out the spherical shape, while the samples remained fixed in terms of both displacement and rotation. These samples were cut into spheres in the diameters of 30–50 mm, with an interval of 5 mm.

In order to evaluate the sphericity of samples, the diameters of the spherical samples were allowed to have errors in less than 0.2 mm in different directions. The mass of each spherical sample was also measured after preparation, and compared with the theoretical mass of ideal spheres in the same diameter, as shown in Fig. 5. Therefore, the feasibility and credibility of this experiment can be guaranteed due to the high sphericity.

The experiment was carried out on an MTS testing machine. The loading rate was set as 0.04 mm/min, and a high-rigidity steel plate loading block was used during the loading process. Each sample was loaded in the sampling direction to reduce the error caused by the anisotropy of the rock. Meanwhile, an extensometer was used to measure the displacement of the sample in the loading direction.

3.2. Loading characteristics and failure modes

The geometric parameters and experimental results are shown in Table 2. As shown in Table 2, the tensile strength obtained by Eq. (12) of rock spheres is almost consistent with the tensile strength obtained by Eq. (13) from Brazilian tests.
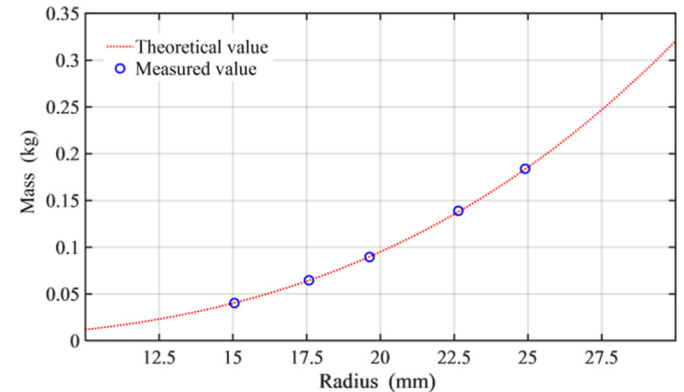

Fig. 4. Influence of the contact angle θ_0 on the normalized stress $2\pi\sigma a^2/F$ distribution in the sphere (Poisson's ratio = 0.2, all stresses are normalized with $F/(2\pi a^2)$).


Fig. 5. Comparison between the measured and theoretical values of the mass of rock spheres.

Table 2
Experimental results of the point loading experiments.

Sample No.	r_s (mm)	Mass (g)	Peak load (kN)	Peak axial displacement (mm)	S_t (MPa)
S30	15.03	40.2	3.6606	0.3627	3.646
S35	17.5	63.4	4.4679	0.3838	3.283
S40	19.57	88.1	5.2655	0.4096	3.093
S45	22.54	140.2	6.4725	0.4473	2.866
S50	25.08	186.3	8.8171	0.5224	3.154

Note: $r_s = (r_x + r_y + r_z)/3$, in which r_x is the radius in x-direction, r_y is the radius in y-direction, and r_z is the radius in z-direction; and S_t is the approximate tensile strength calculated by Eq. (12).

(a)


— Main crack
--- Secondary crack

(b)

(c)
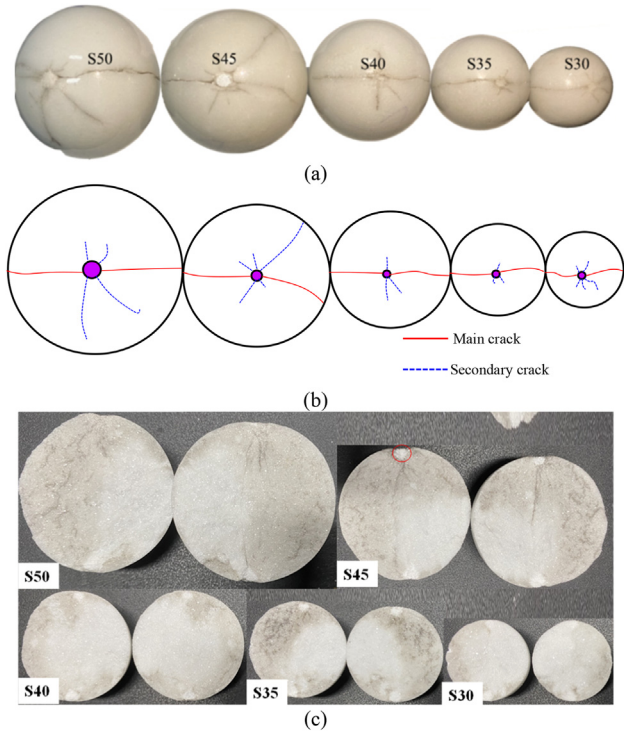
Fig. 6. Images of spherical rock samples after point loading experiments: (a) Cracks on the rock spheres, (b) Sketch of cracks on rock spheres, and (c) Samples splitting into two pieces.

$$S_t = 1.4F / \left(2\pi a^2\right) \tag{12}$$

$$\sigma_t = 2F/(\pi D t) \tag{13}$$

where S_t is the tensile strength obtain by paired point load, and σ_t is the tensile strength obtain by Brazilian tests. The fracture patterns of test samples are shown in Fig. 6. A group of main cracks are formed to split the specimens into two pieces, and thus the specimens lose their load-bearing capacity. Meanwhile, the fracture plane is approximately flat with little debris, which is a typical tensile failure characteristic. Moreover, a crushed zone containing obvious microcracks is generated around the loading points.

These represent both the failure modes (i) and (ii). The crushed zone is first formed due to large compressive stress $(\sigma_{rr})_{\theta\,=\,0}$ and $(\sigma_{\theta\theta})_{\theta\,=\,0}$ near the loading points. Tensile stress $(\sigma_{\theta\theta})_{\theta=0}$ distributes at the edge of compressive stress concentrated area, which drives the main crack to initiate and propagate along the radial direction of the specimen, finally splitting the sample into two pieces.
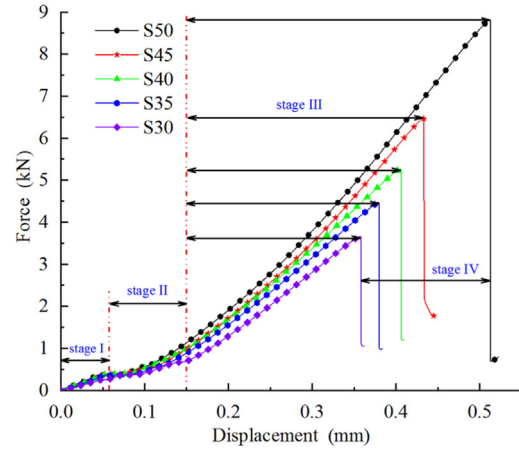
Fig. 7. Displacement-load curves for rock spheres in different diameters under a pair of diametral point loads.
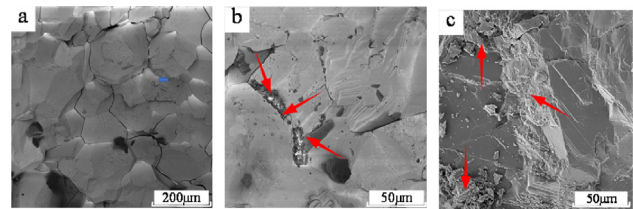
Fig. 8. SEM images of marble samples: (a) Slice of the specimen before failure, (b) Slice of tensile failure zone, and (c) Slice of crushed zone. Red arrows indicate the debris caused by each failure mode.
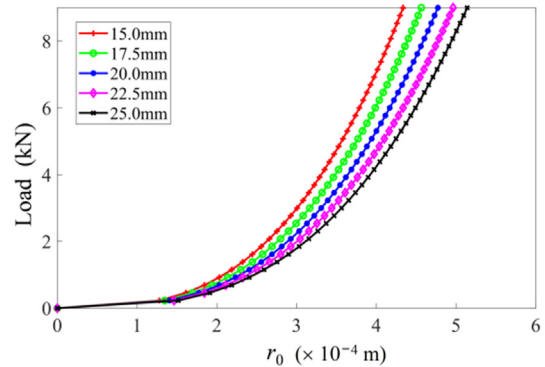
Fig. 9. Relationship between the load and radius of contact circle under different sample sizes.

Fig. 7 shows the load-displacement curve of each sample. As the diameter of a sphere increases, the peak load and the axial displacement increase. There are four stages (Stages I-IV) of the load-displacement curve. At the Stage I, areas near the loading points at both ends are compacted, and the contact area gradually increases under stress which closes the microcracks. The contact area changes from a point to a circular area. At this stage, no macrocrack emerges on the sample. At the Stage II, rock within the contact circle is crushed, producing a macrocrack that propagates to the tip of the crushed zone, accompanied by gently increased loading force. At the Stage III, tensile cracks begin to occur between the center of the sample and crushed zones due to the increased $(\sigma_{\theta\theta})_{\theta=0}$, and the loading force continues to increase until the cracks completely penetrate the sample. At the Stage IV, the sample loses the load-bearing capacity and the loading force drops sharply.

In order to further evaluate the microstructure damage of the sample, the sample before and after failure was scanned using the scanning electron microscope (SEM). Fig. 8a presents the original intergranular structure of marble. The particle size is about 200 µm, and the bonding between the particles and the original gaps can be clearly observed. Fig. 8b and c presents the breakage of bond between particles and the undulating fracture planes, which are characterized by (b) tensile failure and (c) shear failure.

3.3. Contact angle θ_0 and crushed zone

According to the Hertzian contact theory (Timoshenko et al., 1970), when two spheres are in contact under load F, the radius of the contact circle can be obtained as

$$r_0{}^3 = \frac{3R_1R_2}{4(R_1+R_2)}\left(\frac{1-\nu_1^2}{K_1}+\frac{1-\nu_2^2}{K_2}\right)F \tag{14}$$

where R_1 and R_2 are the radii of each sphere; and ν_1, ν_2, K_1 and K_2 are the elastic constants of the spheres. In this experiment, the loading plate can be regarded to have $R_1 \to +\infty$, then Eq. (14) can be written as

$$r_0{}^3 = \frac{3R_2}{4}\left(\frac{1-\nu_1^2}{K_1}+\frac{1-\nu_2^2}{K_2}\right)F \tag{15}$$

The relationship between the load and radius of contact circle under different sample sizes is shown in Fig. 9. It can be seen that with the increase of sample size under the same load condition, the radius of contact circle increases which agrees well with the experimental result. The contact angle can be written as

$$\theta_0 = \arccos\left[\sqrt{3\frac{3}{4R_2^2}\left(\frac{1-\nu_1^2}{K_1}+\frac{1-\nu_2^2}{K_2}\right)F}\right] \tag{16}$$

As loading proceeds during the experiment, the contact area between the loading platen and the spherical sample expands into a circle. It is obvious that r_0 increases with the increase of R_2 and F. The geometric relationship between the deformation of the sphere

and the contact circle can be depicted in Fig. 2b. The contact angle θ_0 and contact radius r_0 are expressed by the deformation of the sphere in the radial direction. In order to further evaluate the relationship between the contact angle and the failure mode of the sphere, the area of the crushed zone of each sample was measured, as shown in Fig. 10b.

Assuming that the plastic deformation of the specimen prior to damage is not taken into account, according to Fig. 10a, the contact angle can be approximately expressed as

$$\theta_0 = \arccos\left(1 - \frac{0.5\Delta r}{a}\right) \tag{17}$$

where Δr is the radial deformation of the sample.

Substituting the measurement data in Table 2 into Eq. (16), the contact angle θ_0 can be calculated. The relationships between the radius (diameter), contact angle and peak load, ratio of the length of the crushed zone in this experiment is shown in Fig. 11.

In Fig. 11a, with the increase in the radius of the sphere, the contact angle increases, which is consistent with the Hertzian contact theory. Moreover, as mentioned in Section 3.3, the peak load increases with the radius, so does the contact angle. Fig. 10b illustrates that the ratio of the crushed zone increases with the increase of the diameter. The relationship between the ratio of crushed areas, contact angle and peak load is shown in Fig. 11c. It is indicated that the proportion of crushed areas increases with the increase of the contact angle, manifesting the same trend at damage points in Brazilian disc experiments based on the Mohr–Coulomb (M–C) criterion and Hoek-Brown failure criterion (Garcia-Fernandez et al., 2018). In addition, the peak load also increases with the increase of contact angle, exhibiting consistency with the result in Kourkoulis et al. (2013) on the contact problem in standardized Brazilian disc tests. The experimental results show that the crushed areas are distributed at $(0.19-0.27)R$ at both ends of the sphere, which is comparable to theoretical results where the crushed zones are distributed between $(0.14-0.2)R$. This is because rocks are considered isotropic in the theoretical calculations, but rocks in the experiments exhibit anisotropy, and the crushed zone of the sphere is larger than that in theoretical calculation due to the end-friction effect.

3.4. Energy dissipation

The external work in the experiment was calculated by multiplying the applied load by the displacement. According to the load-displacement curves obtained during the experiment, the work applied to the samples can be calculated using the method proposed by Mahanta et al. (2017). The strain-energy release rate is defined as the energy dissipated per unit increase in an area during crack growth (Griffith, 1920) and is represented by G. The work done by the testing machine on each sample is shown in Fig. 12.

As shown in Fig. 12, the total work applied to rock spheres increases greatly as the radius increases. The reason may be that with the increase of the sample size, the value of the stress at the crack tip becomes smaller. Then, more energy is consumed in crushed zone at both ends.

The energy dissipations in each failure mode are different. The total work applied to samples (E_{tot}) can be summed up as

$$E_{\text{tot}} = \sum_{i=1}^{2} A_i G_i \tag{18}$$

where i represents the number of failure modes; and A_i and G_i are the fracture area and dissipated energy in each failure mode,
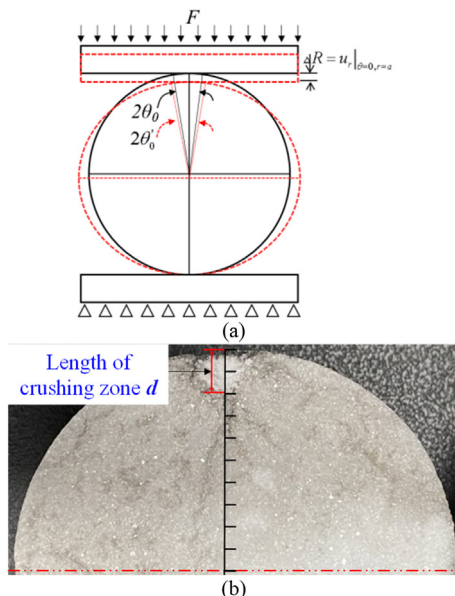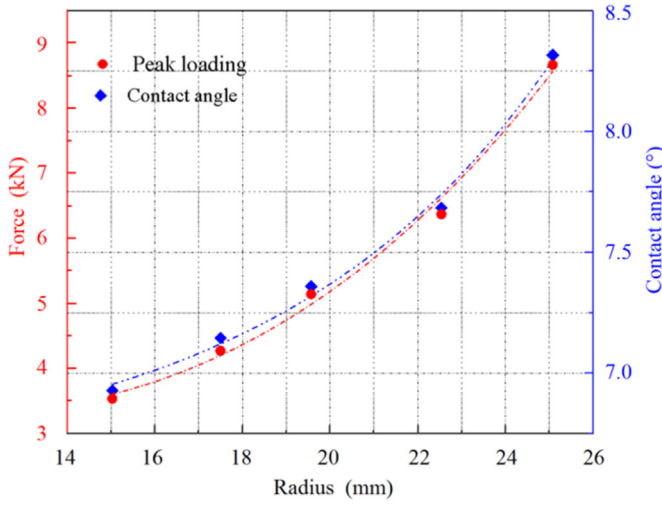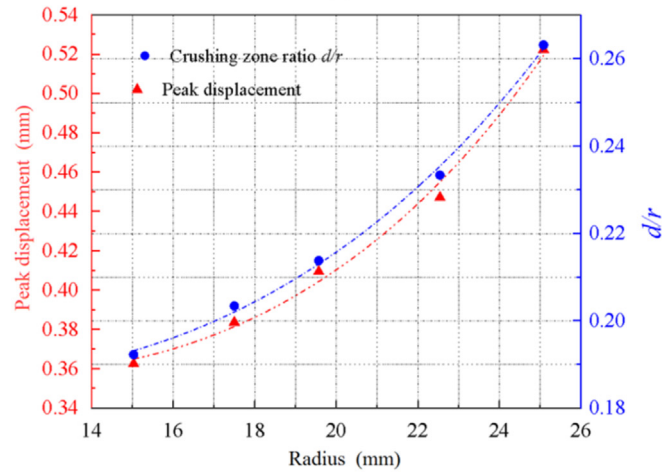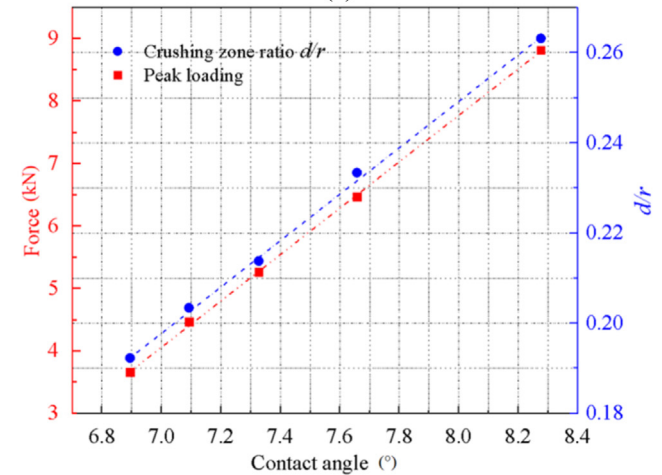

Fig. 10. (a) Schematic diagram of rock axial deformation during loading, and (b) Images of a rock sphere showing the length of the crushed zone.
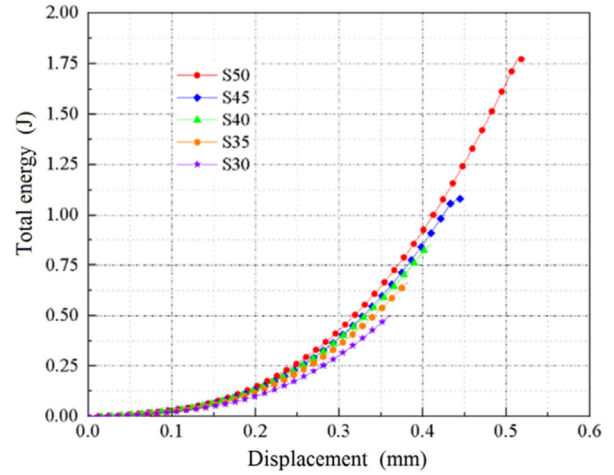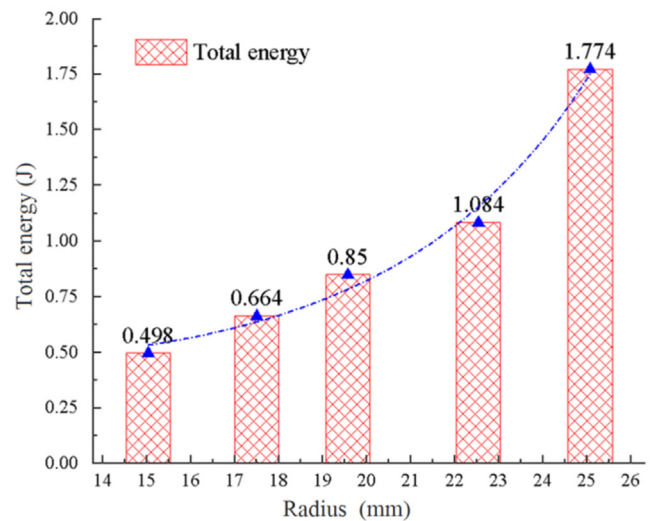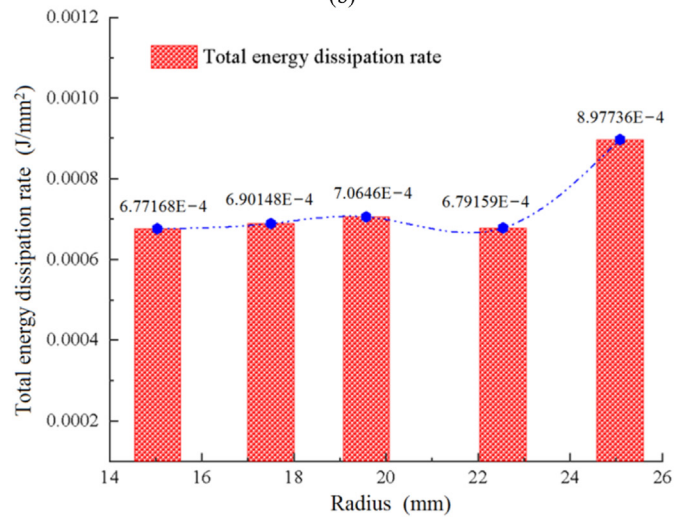
(a)

(b)

(c)

Fig. 11. (a) Relationship between contact angle, peak load, and sample size; (b) Relationship between the sample size, ratio of the crushed zone, and peak displacement; and (c) Relationship between contact angle, ratio of crushed zone, and peak load.

(a)

(b)

(c)

Fig. 12. The work done by the testing machine on each sample: (a) Total energy versus displacement, (b) Total energy versus radius and exponential fitting, and (c) Histogram of the total energy dissipation rate G_{tot}.

respectively. The failure mode is distinguished by the different types of damage surfaces on the specimens. Therefore, there are five experimental dates and two undetermined variables. We can solve the over-determined equation by the least squares method.

The approximate solution of dissipated energy of each fracture can be computed as $G_1 = 0.000294$ J/mm^2 and $G_2 = 0.00865$ J/mm^2.
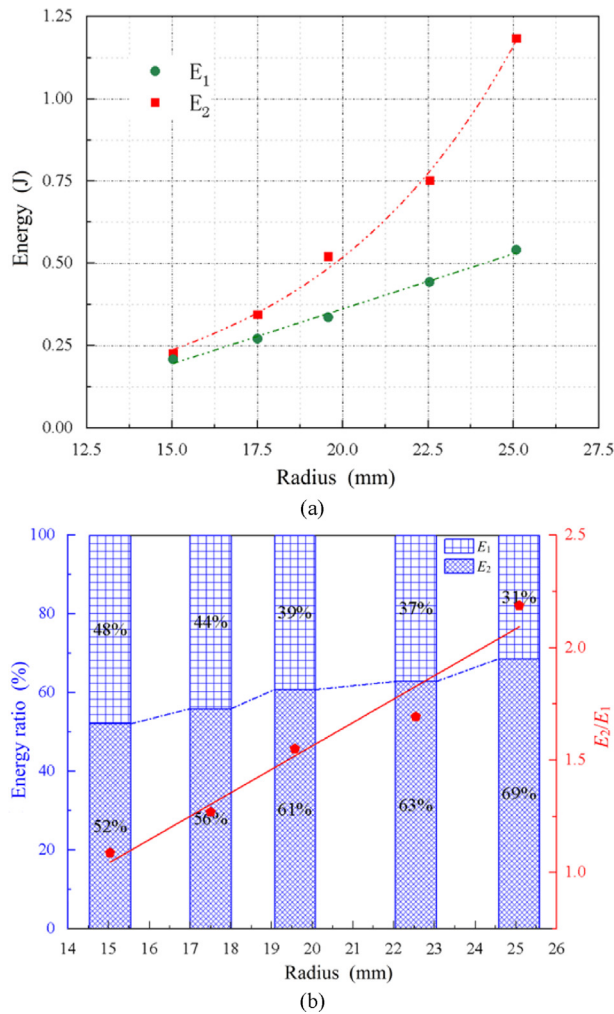
Fig. 13. Energy dissipation in the point loading experiment: (a) E_1 and E_2 versus radius; and (b) Percentage of E_1, E_2, and E_2/E_1 (red point and line).

As the energy required for these two failure modes is given, the energy consumed in rock failure during the experiments can be calculated. The ratios of the energy consumption in shear failure (E_2) and tensile failure (E_1) are introduced as indicators for evaluating the energy dissipation in the experiments.

As presented in Fig. 13, the radius is an important factor affecting the energy distribution in the experiment. Both E_2 and E_1 increase with the increase of the radius. The value of E_1 increases linearly, whereas that of E_2 increases faster. E_2 always accounts for the largest part of the total energy regardless of the sample size, as shown in Fig. 13b. The ratio of E_2/E_1 is always greater than 1, which also agrees well with the experimental results, indicating that most of the energy is consumed in forming crushed zones. In this situation, as the radius increases, the proportion of energy required in creating crushed zones becomes higher. It can be concluded that the larger the size of the sample, the more energy needed to form crushed zones at both ends of samples.

4. Numerical simulation

The analytical solution of stress distribution within point loaded spheres and experiments of paired point loading on marble spheres are presented above. The failure mode of the specimen and the displacement load curve show that failure modes (i) and (ii)

occurred in the experiment. However, the dynamic fracturing process of the sample cannot be directly obtained during the experiment. For this, the DEM-based software PFC3D was used to model the dynamic failure characteristics of rock spheres under point loads. The parallel bonding model was adopted to represent the contact behavior between neighboring individual particles. Before simulating paired point loading on rock spheres, the numerical model was verified through uniaxial compression test to ensure the accuracy of the simulation. The typical stress-strain curve and failure mode of the specimen under uniaxial compression obtained by experiment and simulation are shown in Fig. 14a and b. The numerical parameters are listed in Table 3. Moreover, the failure models of sphere in laboratory experiment and numerical simulation are shown in Fig. 14c and d.

As shown in Fig. 14, the results from discrete element simulation are in good agreement with the experimental results. One primary objective of the numerical simulation is to obtain the internal crack development within rock spheres during the loading process. Thus, only one model of rock sphere with a diameter of 50 mm was constructed to analyze the crack development under point loads. In simulation, the number of both shear and tensile cracks was measured throughout the experimental process, as shown in Fig. 15.

Fig. 15 shows the statistics of the number of tensile cracks (T-crack) and shear cracks (S-crack) in the marble sphere during the point loading process. In order to better evaluate the dominance of the two types of cracks in the failure process, the ratio of T-crack and S-crack (T/S-ratio) over time is also shown in Fig. 15. It can be seen from that when the T/S-ratio is less than 1, the shear cracks dominate the sample's damage, which means that the crushed areas at both ends are generated at the stage between points A and C. After the curve passes the point C, tensile cracks appear, and thus the stress distribution in the specimen switches from compressive stress to tensile stress. Meanwhile, numerous tensile cracks grow rapidly. By this time, the T/S-ratio starts to be greater than 1, and the tensile cracks dominate fracturing of the sample until the macroscopic failure occurs. Then, the cracks penetrate the entire sample at point E, and there are plenty of secondary S-cracks formed due to the friction between the rock sphere and loading platens. At this stage, the extension of crack has terminated, and the T/S-ratio begins to decrease, albeit it remains higher than 1.

In addition, the distribution of the transverse displacement in the specimen at different stages was obtained in numerical simulation as shown in Fig. 16. It can be clearly seen that the displacement is distributed symmetrically along the loading axis until the specimen fails. It can be seen in Fig. 15 that the displacement at both sides of the loading point is greater than other positions due to the end-friction effect. At the beginning of loading, the displacements on both sides are distributed in opposite directions, and the middle part of the specimen is subjected to tensile stress. As the load increases, the compressive stresses at both ends increase, which causes the specimen to break near the loading points at both ends and produce a crushed zone. This process corresponds to the stages A-C in Fig. 16 and Stage II in Fig. 7. Furthermore, after the crushed zone is generated at both ends, macroscopic tensile cracks are generated at the end of the crushed zone, which leads to the overall failure of the sample and loss of bearing capacity.

5. Discussion

The diameter of the sphere directly affects the contact angle between the loading plate and the sphere, and the contact angle has a great influence on the stress distribution near the loading points. As the failure of the specimen is dominated by the stress, Garcia-Fernandez et al. (2018) used the truncated Mohr−Coulomb
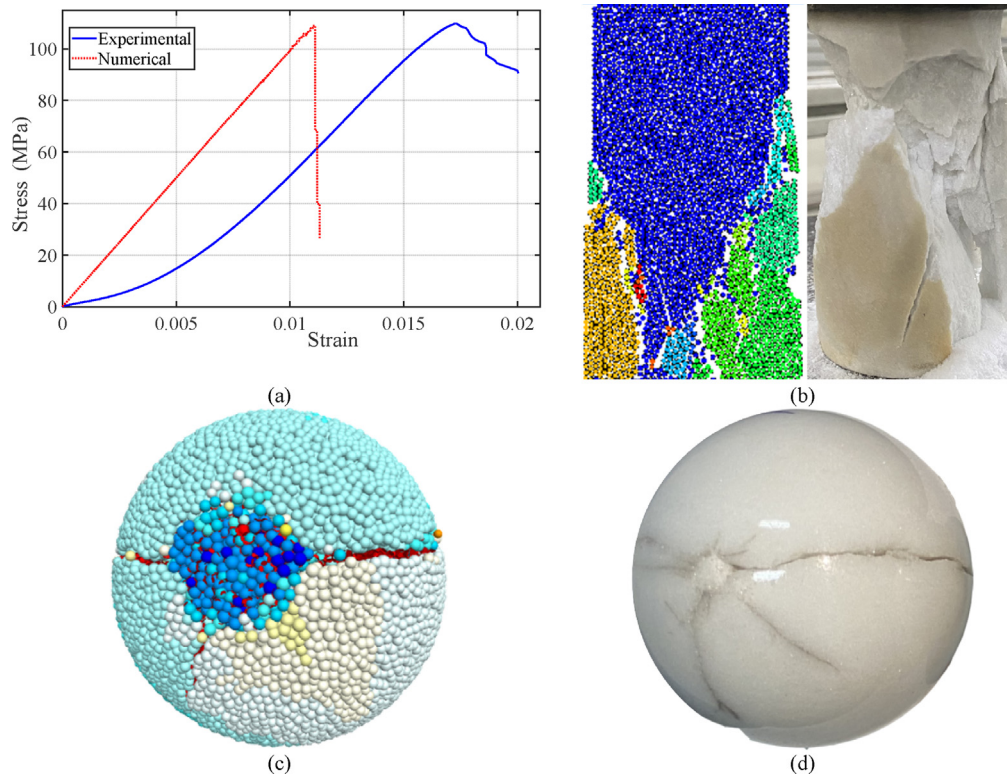
Fig. 14. Numerical verification of uniaxial compression test: (a) Experimental and simulated stress-strain curves, and (b) Simulated and experimental failure modes. Destruction of spherical samples in (c) numerical simulation, and (d) laboratory experiment.

(TMC) and Drucker-Prager criteria to determine the initial failure point of the sample in the Brazilian disc. The result showed that the failure of the Brazilian disc begins from the area between the center and the loading point of the specimen, and the distance between the initial failure point and the loading point increases with the increase of the contact angle. Obtaining the initial crack point is important for determining the damage of the specimen with tensile or compressive stress, and further obtaining the relevant mechanical parameters of the rock. Therefore, considering $\sigma_{\theta\theta}$ and σ_{rr} as the maximum and minimum principal stresses in this work, the M − C and Griffith theories are used to analyze the initial failure point and failure mode in the spherical specimen. When $\sigma_t = 3.7$ MPa, the stress state calculated by Eqs. (7) and (8) on the principal stress plane of the spheres along the loaded diameter is shown in Fig. 17. The M − C criterion is adopted to evaluate the compressive-shear failure of materials, whilst the Griffith criterion is widely applied to tensile failure. As shown in Fig. 17, according to the M − C criterion, the increase in the diameter of specimen can be equivalently considered to be an increase in the contact angle (see Section 3.3). Therefore, the initial failure position gradually approaches the center of the sphere. Besides, failure initiates in a region of about $(0.8-0.86)R$ away from the center. When the diameter of the sample is 50 mm, the initial failure of the sample is tensile type. Based on the Griffith criterion, the initial failure of specimen is caused by compressive stress close to the loading points and failure initiates in a region of about $(0.92-0.97)R$. Moreover, the force-displacement curve (Fig. 7) obtained in the test and the crack statistics (Fig. 15) in the numerical experiment indicate that there is a crushed zone occurring firstly near the loading point, followed by the tensile failure, which can be seen in the numerical simulation. According to the Hertzian theory, under the

Table 3
Micro-parameters of PFC model.

Micro-parameter	Value
Density	2700 kg/m^3
Min-particle size	5.5×10^{-4} m
Normal stiffness, kn	1×10^8 Pa
Shear stiffness, ks	5×10^7 Pa
Linear modulus, $emod$	2.12×10^9 Pa
Parallel-bond modulus, pb_emod	8.02×10^9 Pa
Ratio of normal to shear stiffness of the particle, $kratio$	2.6
Normal parallel-bond cohesion, pb_ten	5.16×10^7 Pa
Shear parallel-bond cohesion, pb_coh	4.3×10^7 Pa
Parallel-bond friction angle, $pb\text{-}fa$	45°

same loading conditions, as the radius increases, the contact angle increases. Theoretically, the increase in contact angle leads to an increased in the compressive stress concentrated areas in the spherical specimen as shown in Fig. 4. Therefore, the energy consumption of shear failure increases, so does the ratio of crushed zone in the experiment. In point loading, the compressive stress concentration near the loading point and the tensile stress below the loading point can affect the failure mode of the specimen, especially at small Poisson's ratio and contact angle. These inhomogeneous stress distributions affect the accuracy of the experimental results; however, the effects of these stresses cannot be completely eliminated. A large/small contact angles will overestimate/underestimate the tensile strength of the rock in the point load test. Thus, the impact of large tensile stress concentrations on the rock strength can only be reduced by selecting a reasonable contact angle.
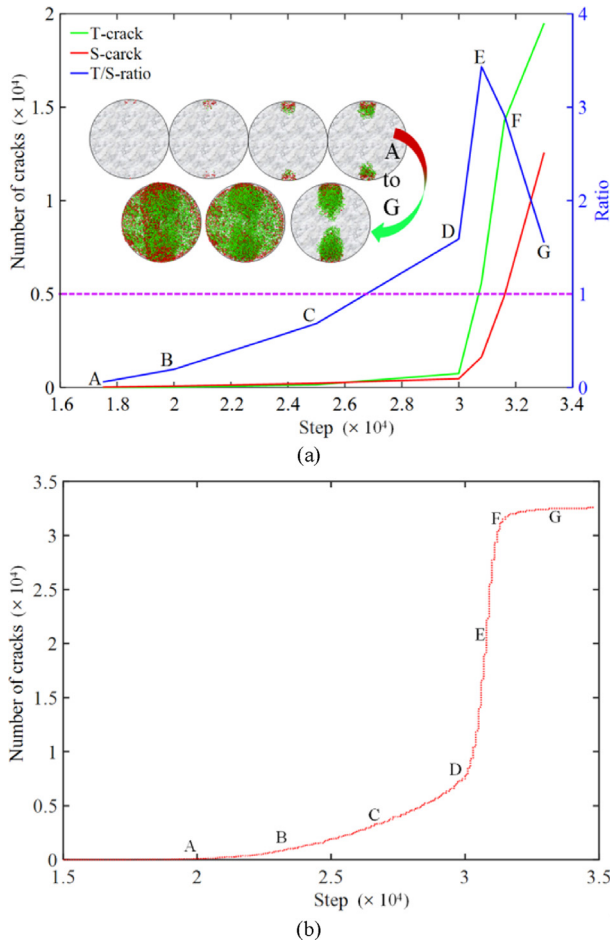
(a)

(b)

Fig. 15. (a) Statistics of shear and tensile cracks, and (b) Evolution of the total crack number.
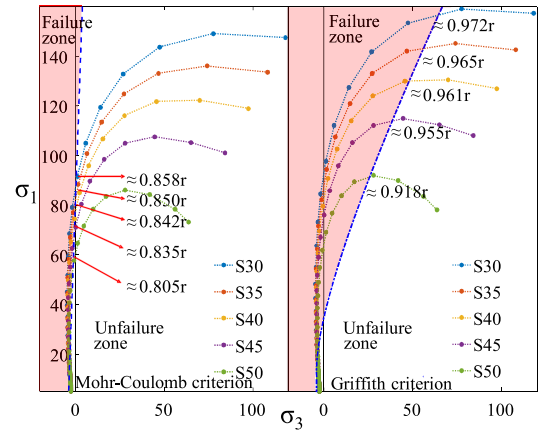

Fig. 17. Evaluation of stress along the central vertical cross section of rock spheres based on the M − C and Griffith criteria (Note that the stress components are normalized with $F/2\pi a^2$). σ_1 and σ_3 are the maximum and minimum principal stresses, respectively.

In study of Brazilian disc experiments, central cracking was used as the available tensile strength judgment (Li et al., 2020). As point load test, Franklin (1985) proposed typical modes of failure for valid and invalid diametral and axial point load tests on cylindrical and irregular sample. Regardless of the Brazilian discs test or point load experiment adopted in the tension test, the contact angle has an effect on the experimental results in terms of failure mode and load characteristics. However, point load tests on rocks are sensitive to the contact angle and Poisson's ratio, and it is tedious to select different contact angles for different Poisson's ratios. Thus, it is not recommended to use point load tests to obtain strength indices of rocks (i.e. tensile strength) in projects that require highly-precise strength parameters of rock masses. In addition, according to the theoretical solution of the point load, the aspect ratio of the
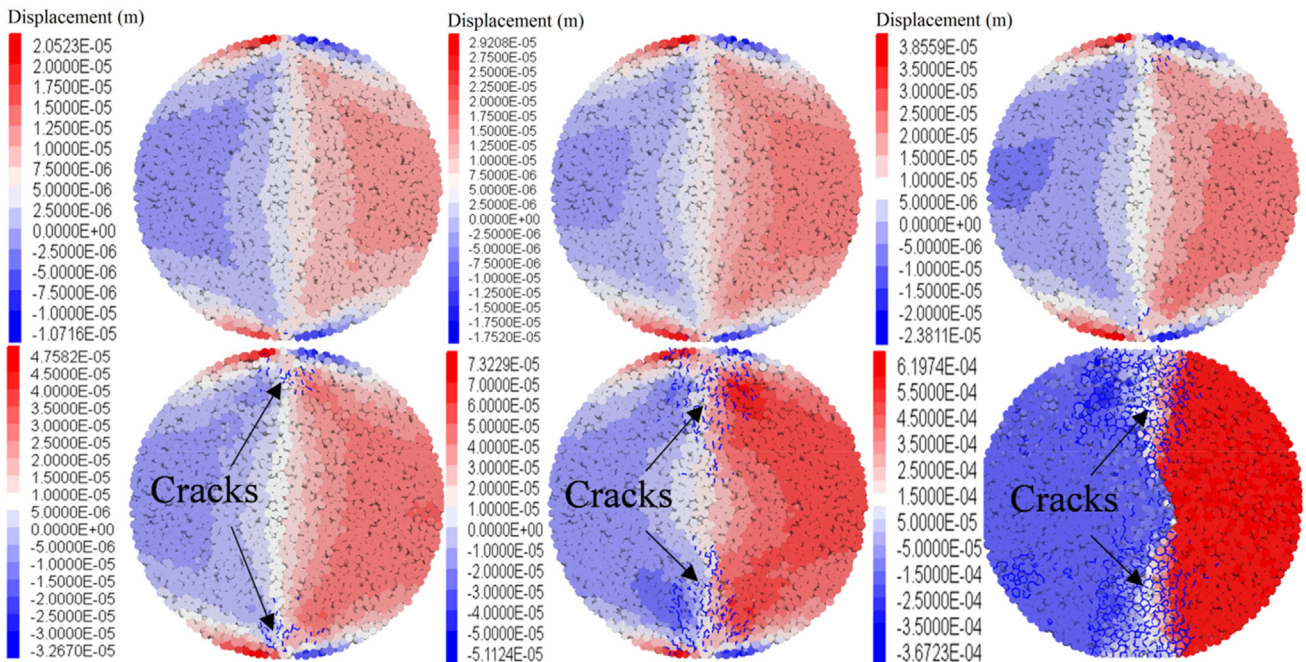

Fig. 16. Simulated horizontal displacement and crack distribution in the rock sphere (Increased number of cracks with increased loading time).

specimen should also be considered when choosing the specimen. It is best to choose a specimen with an aspect ratio close to 1:1.

6. Conclusions

Through theoretical calculations and experiments, the stress distribution and failure characteristics of spherical samples under paired point loads were obtained. The DEM-based software PFC3D was used to simulate the internal failure process of the sample. The following conclusions can be drawn:

(1) The rock sphere is broken into two pieces under point load, accompanied by crushed areas at the ends of the loading and numerous tensile sections in the interior, which can be used as a reference for the rock failure under point loads, and is important for evaluating point load indicators.
(2) The influence of the sample size on the damage of the sample is mainly reflected by the contact angle between samples and the loading platen, which affects the stress distribution and compressive stress concentrated area near the loading point and leads to the different failure modes.
(3) As the sample size increases, the contact angle increases. The boundary point between tensile and compression failure approaches the center of the sphere.

Declaration of competing interest

The authors declare that they have no known competing financial interests or personal relationships that could have appeared to influence the work reported in this paper.

Acknowledgments

References

Akbay, D., Altindag, R., 2020. Reliability and evaluation of point load index values obtained from different testing devices. J. South. Afr. Inst. Min. Metall. 120, 181–190.

AlAwad, M.N.J., 2020. Modification of the Brazilian indirect tensile strength formula for better estimation of the tensile strength of rocks and rock-like geomaterials. J. King Saud Univ. Sci. https://doi.org/10.1016/j.jksues.2020.08.003.

Azarafza, M., Ghazifard, A., Akgun, H., Asghari Kaljahi, E., 2019. Geotechnical characteristics and empirical geo-engineering relations of the South Pars Zone marls, Iran. Geomech Eng 19, 393–405.

Brown, E.T., 1981. Rock Characterization, Testing and Monitoring: ISRM Suggested Methods. Pergamon Press, Oxford, UK.

Chau, K.T., 1998. Analytic solutions for diametral point load strength tests. J. Eng. Mech. 8 (875). https://doi.org/10.1061/(ASCE)0733-9399(1998)124.

Chau, K.T., Wei, X.X., 1999. Spherically isotropic, elastic spheres subject to diametral point load strength test. Int. J. Solid Struct. 36 (29), 4473–4496.

Du, K., Li, X., Tao, M., Wang, S., 2020. Experimental study on acoustic emission (AE) characteristics and crack classification during rock fracture in several basic lab tests. Int. J. Rock Mech. Min. Sci. 133, 104411.

Fan, J., Guo, Z., Tao, Z., Wang, F., 2021. Method of equivalent core diameter of actual fracture section for the determination of point load strength index of rocks. Bull. Eng. Geol. Environ. 80, 1–11.

Franklin, J.A., 1985. Suggested method for determining point load strength. Int. J. Rock Mech. Min. Sci. 22 (2), 51–60.

Garcia-Fernandez, C.C., Gonzalez-Nicieza, C., Alvarez-Fernandez, M.I., Gutierrez-Moizant, R.A., 2018. Analytical and experimental study of failure onset during a Brazilian test. Int. J. Rock Mech. Min. Sci. 103, 254–265.

Garrido, M.E., Petnga, F.B., Martínez-Ibáñez, V., Serón, J.B., Hidalgo-Signes, C., Tomás, R., 2021. Predicting the uniaxial compressive strength of a limestone exposed to high temperatures by point load and leeb rebound hardness testing. Rock Mech. Rock Eng. 55, 1–17.

Griffith, A.A., 1920. The phenomena of rupture and flow in solids. Philos. Trans. Royal Soc. A 221 (4), 163–198.

Hiramatsu, Y., Oka, Y., 1966. Determination of the tensile strength of rock by a compression test of an irregular test piece. Int. J. Rock Mech. Min. Sci. 3 (2), 89–90.

Kourkoulis, S.K., Markides, C.F., Chatzistergos, P.E., 2013. The standardized Brazilian disc test as a contact problem. Int. J. Rock Mech. Min. Sci. 57, 132–141.

Li, D., Wong, L., 2012. The Brazilian disc test for rock mechanics applications: review and new insights. Rock Mech. Rock Eng. 46, 269–287.

Li, D., Li, B., Han, Z., Zhu, Q., 2020. Evaluation on rock tensile failure of the Brazilian discs under different loading configurations by digital image correlation. Appl. Sci. 10, 5513.

Mahanta, B., Tripathy, A., Vishal, V., Singh, T.N., Ranjith, P.G., 2017. Effects of strain rate on fracture toughness and energy release rate of gas shales. Eng. Geol. 218, 39–49.

Markides, C.F., Kourkoulis, S.K., 2012. The stress field in a standardized Brazilian disc: the influence of the loading type acting on the actual contact length. Rock Mech. Rock Eng. 45 (2), 145–158.

Rabat, Á., Cano, M., Tomás, R., Tamayo, Á.E., Alejano, L.R., 2020. Evaluation of strength and deformability of soft sedimentary rocks in dry and saturated conditions through needle penetration and point load tests: a comparative study. Rock Mech. Rock Eng. 53 (6), 2707–2726.

Russell, A.R., Muir Wood, D., 2009. Point load tests and strength measurements for brittle spheres. Int. J. Rock Mech. Min. Sci. 46 (2), 272–280.

Şahin, M., Ulusay, R., Karakul, H., 2020. Point load strength index of half-cut core specimens and correlation with uniaxial compressive strength. Rock Mech. Rock Eng. 53 (8), 3745–3760.

Sgambitterra, E., Lamuta, C., Candamano, S., Pagnotta, L., 2018. Brazilian disc test and digital image correlation: a methodology for the mechanical characterization of brittle materials. Mater. Struct. 51 (1), 19.

Timoshenko, S., Goodier, J., Abramson, H., 1970. Theory of elasticity. In: third ed. Int. J. Appl. Mech. https://doi.org/10.1115/1.3408648 37.

Wei, X.X., Chau, K., 2013. Three dimensional analytical solution for finite circular cylinders subjected to indirect tensile test. Int. J. Solid Struct. 50, 2395–2406.

Wijk, G., 1980. The point load test for the tensile strength of rock. Geotech. Test J. 3 (2). https://doi.org/10.1520/GTJ10902J.

Prof. Ming Tao obtained his PhD in Mining Engineering from Central South University, China in 2013. He conducted postdoctoral research in Geotechnical Engineering from The Hong Kong Polytechnic University. As a visiting scholar, he had two years (2011-2013) academic working experience in the University of Adelaide, Australia, one year (2008-2009) in South Africa, and several months in USA and Singapore. His research interests include rock dynamics, wave scattering, and life cycle assessment.